Single-molecule optofluidic microsensor with interface whispering gallery modes

Xiao-Chong Yu[a,b,c,d,1], Shui-Jing Tang[a,b,1], Wenjing Liu[a,b], Yinglun Xu[a,b], Qihuang Gong[a,b], You-Ling Chen[e,2], and Yun-Feng Xiao[a,b,f,g,h,2]

[a]State Key Laboratory for Mesoscopic Physics, School of Physics, Peking University, Beijing 100871, China; [b]Frontiers Science Center for Nano-optoelectronics, Peking University, Beijing 100871, China; [c]Department of Physics, Beijing Normal University, Beijing 100875, China; [d]Applied Optics Beijing Area Major Laboratory, Beijing Normal University, Beijing 100875, China; [e]State Key Laboratory on Integrated Optoelectronics, Institute of Semiconductors, Chinese Academy of Sciences, Beijing 100083, China; [f]Collaborative Innovation Center of Extreme Optics, Shanxi University, Taiyuan 030006, China; [g]Yangtze Delta Institute of Optoelectronics, Peking University, Nantong 226010, China; and [h]National Biomedical Imaging Center, Peking University, Beijing 100871, China

Edited by Douglas Shepherd, Arizona State University, Tempe, AZ; received May 13, 2021; accepted December 23, 2021 by Editorial Board Member John W. Sedat

Label-free sensors are highly desirable for biological analysis and early-stage disease diagnosis. Optical evanescent sensors have shown extraordinary ability in label-free detection, but their potentials have not been fully exploited because of the weak evanescent field tails at the sensing surfaces. Here, we report an ultrasensitive optofluidic biosensor with interface whispering gallery modes in a microbubble cavity. The interface modes feature both the peak of electromagnetic-field intensity at the sensing surface and high-*Q* factors even in a small-sized cavity, enabling a detection limit as low as 0.3 pg/cm^2. The sample consumption can be pushed down to 10 pL due to the intrinsically integrated microfluidic channel. Furthermore, detection of single DNA with 8 kDa molecular weight is realized by the plasmonic-enhanced interface mode.

optofluidic biosensor | whispering gallery microresonator | interfacial molecular detection

Detecting biological molecules and monitoring their dynamics are of crucial importance in biomedical analysis and disease diagnosis (1, 2). Practical applications generally involve complex biological environments, in which an engineered interface is highly desirable to enable the enrichment, detection, and analysis of specific biomolecules (3). Over the past decades, many techniques on interfacial molecular analysis have been developed, such as lateral flow immunoassay, electrochemical analytical techniques, and optical biosensors (4–7). Among them, optical evanescent microsensors, such as microspheres (8, 9), microtoroids (10–14), and nanowaveguides (15–18), have attracted considerable research interest since they can detect unlabeled molecules and monitor their interactions in real time and in situ with ultrahigh sensitivity, fast response, and miniature footprint.

Despite these advantages, potentials of optical evanescent microsensors have not been fully explored. With the peak field intensity confined inside the cavity, these sensors can utilize the weak tail of the evanescent field only on the sensing surface (8, 10–12, 15, 16), thus limiting their sensitivities. Moreover, ultrasmall sample consumption is desired for high-efficiency sensing yet challenging in evanescent microsensors, since they require delicate sample delivery designs such as an additional chamber (9, 12) or a precisely aligned fluidic channel (19, 20). Therefore, an integrated microfluidic platform with ultimate sensitivity is highly demanded.

In this work, we demonstrate an ultrasensitive optofluidic microbubble biosensor by exploiting the whispering gallery modes (WGMs) peaked at the interface between the optical resonator and the analyte solution, which are termed as the interface modes. Previously, the microbubble resonator has been widely used for measuring refractive index, biomolecule concentration, and single nanoparticle generally by the mode localized in the liquid core (21–29). Here, we find that the profile of the WGM field can be tuned by varying the wall thickness, and the interface mode emerges when the maximum of the field intensity is drawn onto the interface. Compared with conventional evanescent sensors, the present scheme utilizing interface modes promises maximum sensitivity for interfacial molecular analysis, pushing the detection limit down to 0.3 pg/cm^2. The scheme is also compatible with the widely adopted techniques to enhance signal-to-noise ratio (SNR) such as plasmonic hybridization (30–33) and frequency tracking (12, 15, 18). As a proof of concept, single-molecule detection is demonstrated with a plasmonic-enhanced interface mode. Naturally integrated into a microfluidic system, the sensor with single-molecule sensitivity exhibits ultrasmall sample consumption down to 10 pL, providing an automatic platform for biomedical analysis.

Results

The optofluidic microbubble biosensor utilizes its inner interface to capture and detect analytes (Fig. 1*A*), and thus the optical field intensity at this interface is crucial to the sensitivity. In

Significance

Optical microresonators have emerged as promising platforms for label-free detection of molecules. However, approaching optimum sensitivity is hindered due to the weak tail of evanescent fields. Here, we report the implementation of the interface modes for ultrasensitive sensing in a microbubble resonator. With the electromagnetic field peaked at the interface between the optical resonator and the analyte solution, interface modes enable sensing of biomolecules with a detection limit of 0.3 pg/cm^2. Single-molecule detection is further demonstrated using the plasmonic-enhanced interface modes. In addition, intrinsically integrated into a microfluidic channel, the sensor exhibits ultrasmall sample consumption down to 10 pL, providing an automatic platform for biomedical analysis.

Author contributions: X.-C.Y., S.-J.T., and Y.X. performed the experiments; X.-C.Y. carried out the simulation and numerical calculation; X.-C.Y., S.-J.T., W.L., Q.G., and Y.-L.C. analyzed the data; X.-C.Y., S.-J.T., W.L., Y.X., Q.G., Y.-L.C., and Y.-F.X. contributed to the discussions and wrote the manuscript; S.-J.T. and Y.-F.X. conceived the idea; and Y.-L.C. and Y.-F.X. supervised the project.

The authors declare no competing interest.

This article is a PNAS Direct Submission. D.S. is a guest editor invited by the Editorial Board.

[1]X.-C.Y. and S.-J.T. contributed equally to this work.

[2]To whom correspondence may be addressed. Email: yfxiao@pku.edu.cn or ylchen@semi.ac.cn.

This article contains supporting information online at https://www.pnas.org/lookup/suppl/doi:10.1073/pnas.2108678119/-/DCSupplemental.

Published February 3, 2022.

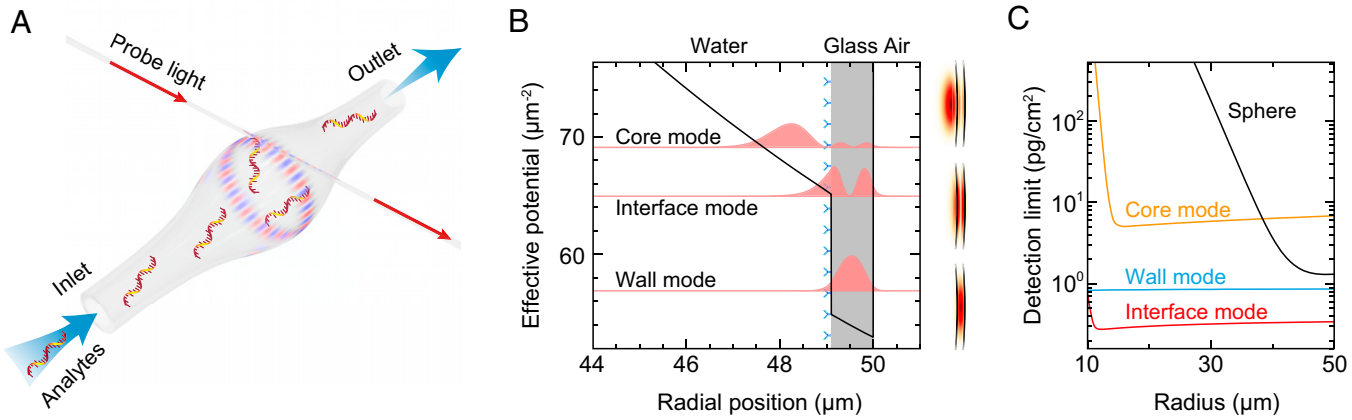

Fig. 1. Optofluidic microbubble cavity for interfacial molecular detection. (*A*) Schematic of the optofluidic microbubble biosensor. Analytes enter the naturally integrated microfluidic channel and are captured by the interior surface of the cavity. (*B*) Effective potential of the microbubble cavity (black curve), radial field distributions (pink curves) of three typical kinds of resonance modes (*Left*), and the corresponding cross-sectional field distributions (*Right*). From bottom to top: wall mode, interface mode, and core mode. (*C*) Minimum detectable surface density of molecules using the interface mode (red curve), wall mode (blue curve), and core mode (orange curve) in a microbubble cavity and the fundamental mode of a microsphere (black curve) as a function of the equatorial radius.

cylindrical coordinates (r, ϕ, z), WGMs of a microbubble cavity can be described by the radial mode number q, azimuthal mode number m, and axial mode number j (*SI Appendix*). The radial field distributions in such a structure can be described by the Helmholtz equation, which is analogous to the time-independent Schrödinger equation (28, 34, 35) with the effective radial potential of the transverse-electric modes written as

$$V(\rho) = \frac{m^2 - 1/4}{\rho^2}, \qquad [1]$$

where $\rho = nr$ with n being the refractive index and r the radial position, and m denotes the azimuthal mode number. Due to the discontinuity of refractive indexes in the radial direction, steep potential barriers exist at the inner and outer surfaces of the silica wall, shown as the black curve in Fig. 1*B*. Depending on the relative magnitude between the effective kinetic energy k_q^2 of the WGM with radial mode number q and the barrier height at the sensing interface V_{int}, the WGMs can be classified into three types, wall modes, interface modes, and core modes, as follows: 1) When $k_q^2 < V_{\text{int}}$, optical fields are concentrated in the silica wall, forming the wall modes; 2) when $k_q^2 > V_{\text{int}}$, optical fields are localized in the liquid core, forming the core modes; and 3) when $k_q^2 \approx V_{\text{int}}$, a special mode family emerges with the field peak located exactly at the interface between the silica wall–liquid core, termed the interface mode. The three types of modes are suitable for different applications. For example, wall modes can be used for temperature sensing with less environmental disturbance (36), while core modes are advantageous for refractive index monitoring and nanoparticle detection inside bulk solutions (26–28). In particular, interface modes ensure the maximum sensitivity for interfacial molecular detection and analysis.

Theoretically, analytes adsorbed on the inner surface of a microbubble cavity introduce a resonance wavelength shift $\delta\lambda$, which could be obtained by (*SI Appendix*)

$$\frac{\delta\lambda}{\lambda} = D n_s \sigma \frac{\mathrm{d}n_s}{\mathrm{d}C_s}, \qquad [2]$$

where λ is the resonance wavelength, n_s is the refractive index of the analyte solution ($n_s \approx 1.33$ for the aqueous solution with low analyte concentration), and σ and C_s denote surface mass density for analyte adsorbed on the sensing surface and the concentration of analyte solution. For typical biological molecules, refractive index increment $\mathrm{d}n_s/\mathrm{d}C_s \approx 0.2\,\mathrm{cm}^3/\mathrm{g}$ (37). The parameter $D = \iint \varepsilon_0 |E|^2 \,\mathrm{d}S / 2U$, in which ε_0 is the vacuum permittivity, E is the electric field magnitude, and U represents the total energy stored inside the resonator. The smallest detectable resonance shift is typically $1/50$ to $1/100$ of the mode linewidth $\Delta\lambda$ reported in previous works (15, 38–40), also confirmed in our experiment (*SI Appendix*, Fig. S8). Thus, here a resolution of $\Delta\lambda/50$ is used to quantitatively estimate the detection limit of the microsensor. As shown in Fig. 1*C*, compared with the core mode and the wall mode, the interface mode exhibits a much lower detection limit in surface density down to 0.3 pg/cm^2. The detection limit remains nearly unchanged even when the equatorial radius of the microbubble approaches 10 μm, where sample with volume down to 10 pL can be analyzed by the naturally integrated microfluidic channel. In comparison, for typical evanescent microsphere sensors, the detection limit deteriorates exponentially when the cavity radius is below 45 μm due to the strongly reduced Q factor. In addition, the detection limit of molecular concentration can be estimated according to the binding affinity between the analyte molecules and the functionalized cavity surface (*SI Appendix*).

A method has been developed to identify different modes through the thermo-optic effect. Characterized by different field profiles, the three kinds of modes exhibit distinctive thermal responses to temperature disturbance δT, which can be described as

$$\frac{\delta\lambda}{\lambda} = \left(\sum_i \frac{\alpha_i f_i}{n_i} + \beta_{\text{silica}} \right) \delta T, \qquad [3]$$

where i = liquid, silica, or air; α_i, f_i, and n_i are the corresponding thermo-optic coefficient, energy distribution ratio, and refractive index; and β_{silica} denotes the linear expansion coefficient of the silica wall. Different types of modes can be classified by their energy ratio in the liquid core f_{liquid}. According to numerical analysis (*SI Appendix*), for the microbubble resonator with wall thickness of 0.5 to ~2.5 μm, $0.1 < f_{\text{liquid}} < 0.4$ for low-order interface modes, while $f_{\text{liquid}} < 0.1$ and $f_{\text{liquid}} > 0.4$ for the wall and core modes, respectively. Explicitly, as $\alpha_{\text{liquid}} = -9.16 \times 10^{-5}\,\mathrm{K}^{-1}$ and $\alpha_{\text{silica}} = 1.19 \times 10^{-5}\,\mathrm{K}^{-1}$, core modes have the strongest and negative thermal shifts; on the contrary, wall modes manifest weak and positive thermal shifts; and interface modes, distributed in both silica and water, generally present weak and negative thermal responses.

Experimentally, a microbubble resonator with the wall thickness of about 1 μm (Fig. 2 *A*, *Inset*) is fabricated from a microcapillary by CO_2 laser irradiation (*Materials and Methods*).

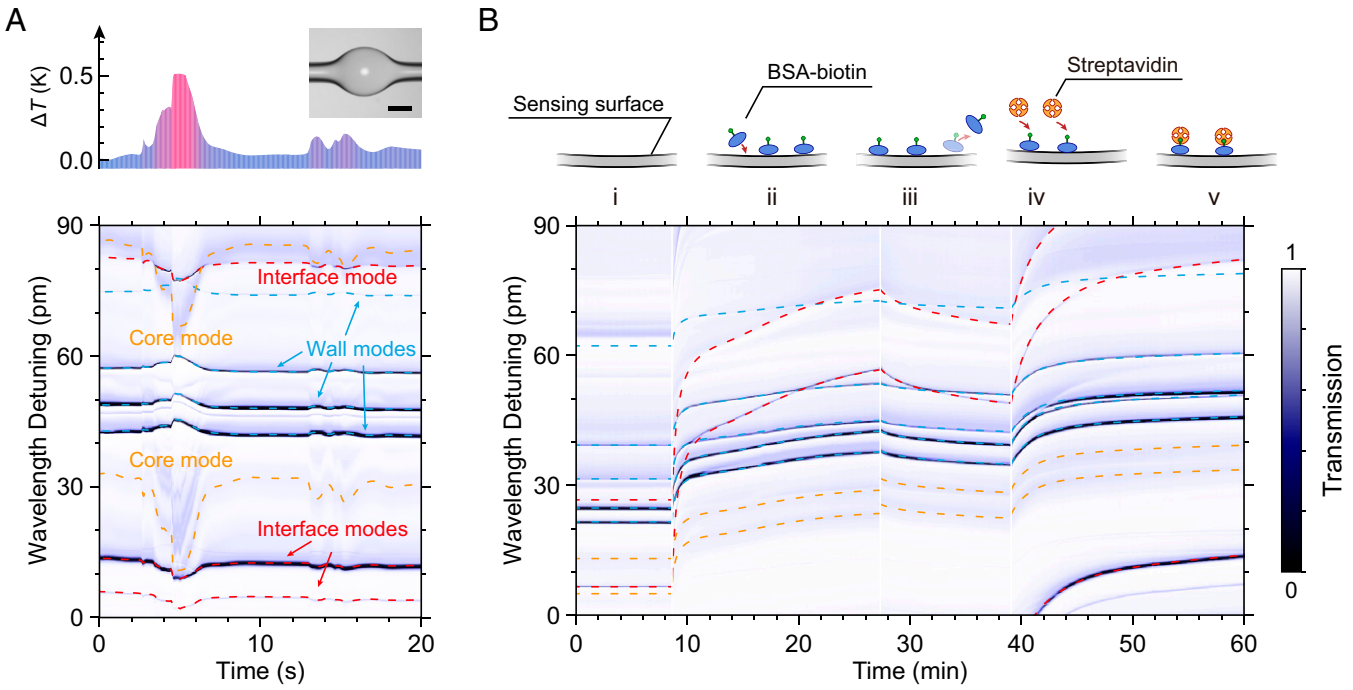

Fig. 2. Interfacial analysis of specific interaction between proteins in an optofluidic microbubble sensor. (*A*) (*Top*) Environmental temperature drift of the microbubble cavity with time. *Inset* shows optical image of the microbubble resonator. (Scale bar: 50 μm.) (*Bottom*) Experimental response of wall modes, core modes, and interface modes during the environmental temperature drift. (*B*) Resonance shifts of the three kinds of modes during the sequential addition of citrate buffer (*i*), biotinylated BSA molecules in citrate buffer (*ii*), citrate buffer (*iii*), and streptavidin proteins in citrate buffer (*iv* and *v*).

The wall thickness of the microbubble cavity can be well adjusted by controlling the microbubble diameter (*SI Appendix*, Fig. S3). WGMs are excited by a tunable laser via a side-coupled tapered fiber, and the transmission spectrum is monitored in real time. After intentionally perturbing the environmental temperature by a local heat source, core modes with the largest thermal shifts are first identified (orange curves in Fig. 2*A*). According to numerical simulations, f_{liquid} of the core mode with the largest thermal shift throughout the mode family is around 1 (*SI Appendix*). Referencing to the core mode, the values f_{liquid} of all other modes are obtained subsequently, according to which different kinds of modes can be identified.

The sensing capabilities of different modes are then characterized by microfluidic experiments with two kinds of analytes, biotinylated bovine serum albumin (BSA-biotin) molecules and streptavidin proteins. To eliminate the influence of environmental thermal fluctuations, the microbubble cavity is kept in a thermostatic chamber. As 1 μM BSA-biotin molecules gradually enter the microfluidic channel, all WGMs experience red shifts (Fig. 2 *B*, *ii*) due to the molecular adsorption onto the hydroxylated silica surface. After removing the surplus BSA-biotin molecules with citrate buffer rinsing (Fig. 2 *B*, *iii*), streptavidin proteins with the concentration down to 50 nM are then delivered into the microbubble cavity. Further red shifts occur due to specific binding between the two kinds of molecules (Fig. 2 *B*, *iv*). In addition, the specific interaction is confirmed by two control experiments. First, no evident resonance shift is observed when 150 nM streptavidin proteins is injected into the microbubble cavity without BSA-biotin molecule functionalization (*SI Appendix*, Fig. S4). Second, the interface mode experiences almost the same red shifts when the mixed solutions of 20 nM target streptavidin proteins with and without 180 nM control BSA molecules are injected into the microbubble cavity with BSA-biotin molecule functionalization (*SI Appendix*, Fig. S5).

Relative sensitivities of different modes are extracted from the mode shifts and summarized as a function of the corresponding f_{liquid}, which are also compared with numerical simulations (Fig. 3). In simulation, the wall thickness of the microbubble cavity is scanned between 1.0 and ∼1.2 μm to account for the inevitable nonuniformity during the fabrication process. All the experimental data fall into the zones of the numerical prediction, confirming an at least twofold sensitivity improvement of the

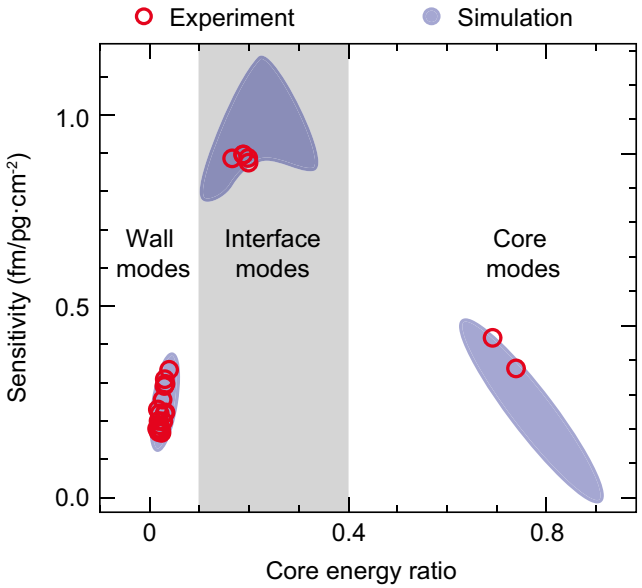

Fig. 3. Interfacial sensitivity of the wall modes, interface modes, and core modes. Shown are experimental (red circles) and numerical (purple shadow) results of the sensitivity versus the energy distribution ratio in the water core of different modes. Parameters for simulation: radial mode number $q = 1$ (wall modes), 2 (interface modes), and 3 (core modes) for the wall thickness of 1.0 to ∼1.2 μm with the azimuthal nonuniformity <0.3 μm.

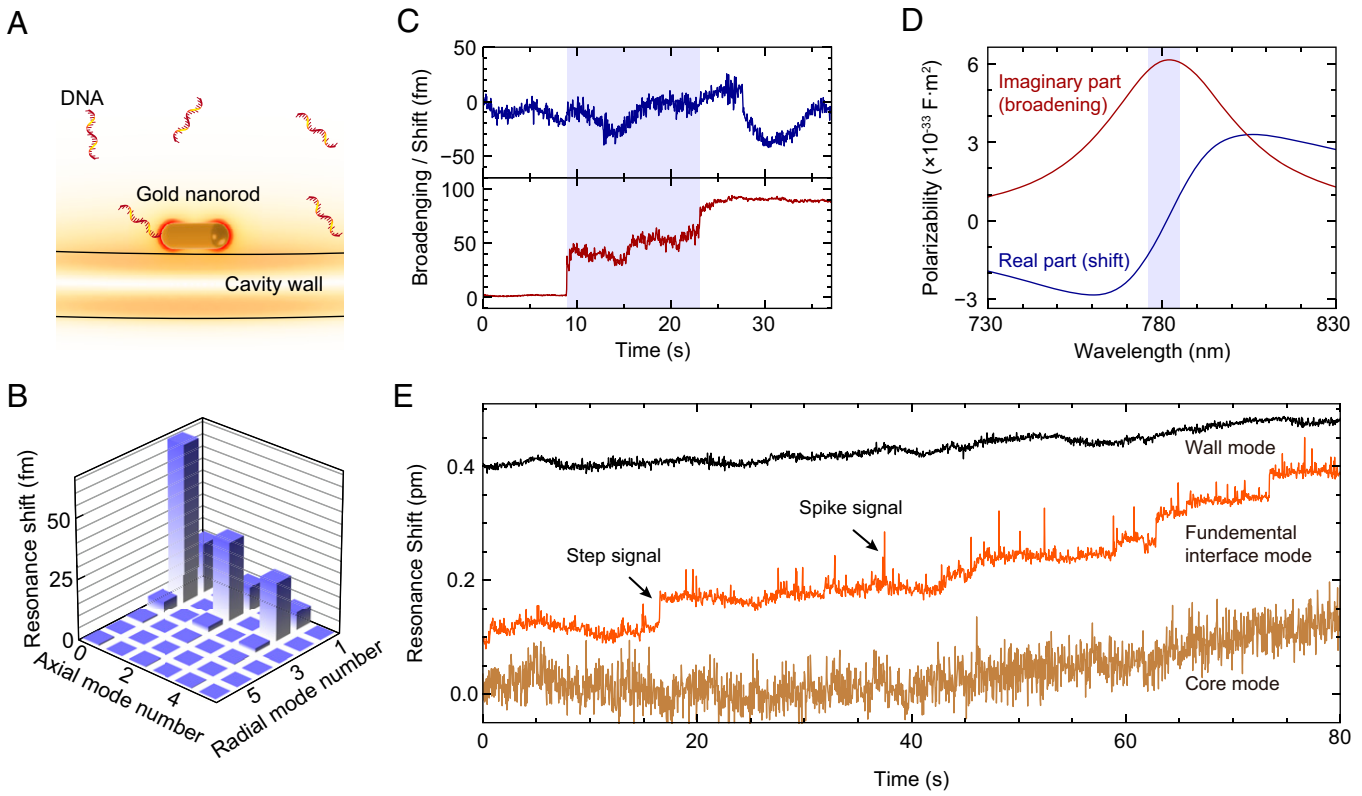

Fig. 4. Single-molecule detection with the plasmonic-enhanced interface mode. (*A*) Schematic of the Au-decorated microsensor. A gold nanorod is functionalized on the interior surface of the microbubble cavity. (*B*) Calculated resonance shifts induced by a single DNA oligo for the modes with different radial and axial mode numbers with plasmonic enhancement. Parameters for the calculation: microbubble wall thickness 0.88 μm, molecular weight 8 kDa, and plasmonic enhancement factor $\gamma_p\gamma_e = 6.25 \times 10^4$. (*C*) Resonance shift and linewidth broadening of fundamental interface mode during the nanorod binding process. (*D*) Real and imaginary parts of the polarizability of the gold nanorod near the plasmonic resonance. (*E*) Resonance shift induced by a single DNA oligo of a fundamental interface mode (orange curve), a wall mode (black curve), and a core mode (brown curve) with plasmonic enhancement.

interface modes compared with both the wall and core modes. With the interface mode of the highest sensitivity, the minimal detectable concentration of streptavidin proteins is deduced to be 1 aM, taking into account the functionalization density and the intermolecular binding affinity (*SI Appendix*).

The proposed scheme is readily compatible with the widely adopted SNR enhancement techniques. Here, single-molecule detection is demonstrated by the plasmonic-enhanced interface mode (Fig. 4*A*). With a gold nanorod adsorbed onto the inner surface of a microbubble, numerical simulation predicts a field enhancement factor $\gamma_p = 2,500$ at the hotspot. An additional plasmonic enhancement factor γ_e at the range of 10^1 to 10^2 has been reported owing to surface roughness of the gold nanorod or the ion layer around the molecules in the aqueous environment (9, 15, 41). In contrast to the collective molecule detection, sensitivity of single-molecule detection relies on both the radial and axial mode numbers of WGMs (*SI Appendix*). As shown in Fig. 4*B*, the fundamental axial interface mode with axial mode number 1 and radial mode number 2 could result in the largest resonance shift. With $m = 8$ kDa and $\gamma_e = 25$, the maximum resonance shift reaches ∼65 fm, which is much higher than the noise level $\sim\Delta\lambda/50 = 15.6$ fm ($Q > 10^6$) due to the frequency fluctuation that mainly arises from the thermal-refractive noise, laser jitter, and $1/f$ technical noise (42, 43). Although there are a few low-order wall modes that have the potential for single-molecule detection, the SNR is very low. The resonance shifts of most wall modes and all the core modes are too small to be resolved the single-molecule signals.

The fundamental interface mode is experimentally identified by combining the aforementioned thermo-optic effect with an axial field mapping technique, in which a taper fiber is scanned along the axial direction to depict the field profile (*SI Appendix*, Fig. S2). Then, the microbubble cavity is functionalized with a gold nanorod while the fundamental interface mode is monitored in real time (*Materials and Methods*). A linewidth broadening without mode shift confirms the adsorption of the gold nanorod, due to the zero real polarizability of the gold nanorod at the resonance condition (Fig. 4 *C* and *D*) (44). The intrinsic Q factor of the fundamental interface mode before and after gold nanorod adsorption is 2.6×10^8 and 8.6×10^6, respectively (*SI Appendix*, Fig. S7).

Single-strand DNA molecules are then delivered into the Au-decorated microsensor. The resonant wavelengths of three representative modes are traced, as presented in Fig. 4*E*. Transient steps and spikes are observed on the trace of the fundamental interface mode, corresponding to the adsorption and the transient movements of single DNA molecules, respectively. In contrast, on the trace of the wall mode and the core mode, single-molecule signals are buried in the frequency noises and difficult to be resolved. The noise levels are 3.1 and 23 fm for the high-Q interface mode with $\Delta\lambda = 0.2$ pm and low-Q core mode with $\Delta\lambda = 2.5$ pm, respectively (*SI Appendix*, Fig. S8). In addition, the quasi-static resonance shift induced by the slow drifting of the laser wavelength is observed with less than 0.1 pm in the period of 30 s. As this drift is slower than any physical processes (molecule adsorption, transient movement, etc.), it is negligible in the sensing experiments.

Single-molecule signals detected by the fundamental interface mode are analyzed statistically. Single-molecule steps and spikes are extracted from the resonance wavelength trace according to

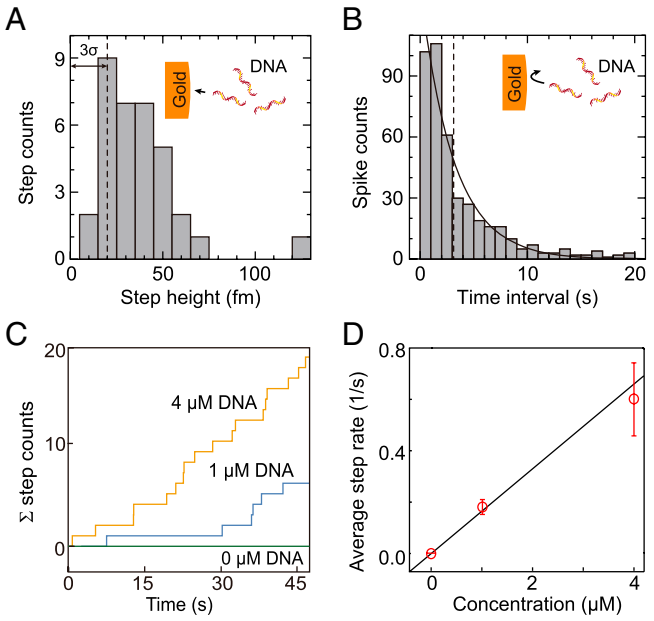

Fig. 5. Statistical analysis of single-molecule signals of the plasmonic-enhanced fundamental interface mode. (*A*) Statistical distribution of step heights induced by the adsorption of single DNA molecules onto the gold nanorod that is placed on the inner surface of the microbubble cavity. (*B*) Statistical distribution of the time interval between two sequential spikes due to the transient movements of single DNA molecules around gold nanorods. (*C*) Cumulative step counts for DNA molecules with different concentrations. (*D*) Average step rates as a function of DNA concentration.

the noise level and summarized in Fig. 5 *A* and *B*, respectively. It can be found that a single-strand DNA molecule with $m \approx 8$ kDa can induce the resonance shift up to ∼70 fm (Fig. 5*A*), revealing $\gamma_e \sim 25$, consistent with the numerical estimation. Both the wall and core modes fail to resolve the single-molecule signals even under such a large plasmonic enhancement factor $\gamma_p\gamma_e = 6.25 \times 10^4$, highlighting the improved sensing capability of the interface mode. Fig. 5*B* reveals that the time interval between spikes follows the exponential distribution with an average value of about 3 s. Furthermore, measurements of DNA molecules with different concentrations illustrate a linear dependence of average step rate on the concentration, indicating that the detected signals are from single-molecule adsorption (45). In addition, replicated experiments confirm the reproducibility of the single-molecule detection (*SI Appendix*, Fig. S9).

In conclusion, we proposed an optofluidic biosensor with the interface modes in a microbubble resonator. The interface mode features both the peak field intensity at the sensing surface and high-Q factors, enabling a detection limit as low as 0.3 pg/cm^2. Furthermore, the proposed scheme can be directly incorporated with other SNR enhancement methods, enabling multifold sensitivity enhancement. As an example, single-molecule detection was demonstrated with the plasmonic-enhanced interface mode. In addition, naturally integrated with the microfluidic system, the optofluidic biosensor allows for rapid biochemical sensing with an ultrasmall sample consumption, and the sensing efficiency could be well adjusted by controlling the flow rate of analyte solution and cavity size (46, 47) (*SI Appendix*, Fig. S6). Combining sample preparation and delivery with the ultrasensitive analysis technique, the biosensor provides a promising platform for ultrasensitive biochemical analysis in practical applications such as biomedical analysis and early-stage diagnostics (48, 49).

Materials and Methods

Microbubble Resonator Fabrication. The microbubble resonator is fabricated from a silica glass capillary (27, 50, 51) (TSP100170, Polymicro). First, the capillary is tapered to a diameter below 40 μm via heating and pulling procedures using a hydrogen flame. Consequently, the tapered capillary is transferred to a holder and pressurized inside to several atmospheres. Two focused CO_2 laser beams are irradiated on the capillary from opposite directions, providing a uniform heating. Finally, with a well-controllable heating power, a microbubble cavity with desired diameter and wall thickness is formed near the focus point. The wall thickness of the microbubble changes with the diameter when a capillary taper is irradiated by a CO_2 laser to form a microbubble cavity, as simulated by finite-element modeling. A microbubble cavity array on a same silica capillary is presented to demonstrate the repeatability of microbubble fabrication (*SI Appendix*, Fig. S3).

Experimental Setup. A microbubble resonator (about 100 μm in radial diameter and ∼1 μm in wall thickness) is integrated in a microfluidic system and probed by a tunable diode laser (780-nm wavelength band; TLB-6712, New Focus) via the tapered-fiber coupling. Real-time transmission spectra are monitored by a photoreceiver (model 1801, New Focus) and recorded using a data acquisition (DAQ) card (USB6251-BNC, National Instruments). The whole system is sealed inside a poly(methylmethacrylate) (PMMA) chamber to minimize environmental disturbance.

Experimental Details for Protein Adsorption. To improve the reusability, the aqueous solution of 0.5 to ∼2 M sodium hydroxide (NaOH) is used to hydroxylate the microbubble inner surface. Slight blue shift (<1 pm/min) of the resonance wavelength for interface modes can be observed due to the surface reaction. The BSA-biotin proteins exhibit efficient adsorption when pH ≈ 5.0 for citrate buffer, which is near the isoelectric point of the BSA protein, while the desorption appears at a higher or lower pH (i.e., phosphate-buffered saline with pH = 7.2 in our experiment) on such a hydroxylated surface. The BSA-biotin (purchased from OKA) and streptavidin (purchased from Sigma-Aldrich) are stepwisely diluted for more precise concentration control.

Gold Nanorod Functionalization. The gold nanorod we used is 10 nm in diameter and 40 nm in length with the plasmonic resonance wavelength at about 780 nm (purchased from nanoseez). The concentration of the gold nanorod solution with positive charges is diluted down to 2 pM to avoid multiple-binding events, and the pH value is controlled using hydrochloric acid (HCl) to enable surface binding. After the injection of the gold nanorod solution, the nanorod starts to collide with and bind to the inner surface of the microbubble. The binding events of gold nanorods can be observed in the imaging system due to the large scattering cross-section. Furthermore, the monodispersion of gold nanorod adsorbed on the microbubble surface can be characterized by the linewidth broadening with zero mode shift (44).

DNA Preparation. The stock solution of thiol-modified DNA oligo (5′-SH-C6-TTTTGAGATAAACGAGAAGGATTGAT-3′, Sangon Biotech) is prepared by dissolving the single-strand DNA oligo into 1× Tris-EDTA (TE) buffer (purchased from Sangon Biotech) to a final concentration of 100 μM. Before the experiment, 10 mM of tris(2-carboxyethyl)phosphine hydrochloride is added to the solution to reduct the thiol agent.

Data Availability. All study data are included in this article and/or *SI Appendix*.

ACKNOWLEDGMENTS. This project is supported by the National Key R&D Program of China (Grant 2018YFB2200401), the National Natural Science Foundation of China (Grants 11825402, 11654003, 62105006, 11974341, and 62035017), and the High-performance Computing Platform of Peking University. X.-C.Y. is supported by the China Postdoctoral Science Foundation (Grant 2018M630020) and the Fundamental Research Funds for the Central Universities. S.-J.T. is supported by the China Postdoctoral Science Foundation (Grants 2021T140023 and 2020M680187).

1. X. Fan, *Advanced Photonic Structures for Biological and Chemical Detection* (Springer, 2009).
2. A. B. Matsko, *Practical Applications of Microresonators in Optics and Photonics* (CRC Press, 2018).
3. A. E. Nel *et al.*, Understanding biophysicochemical interactions at the nano-bio interface. *Nat. Mater.* **8**, 543–557 (2009).
4. C. Cao, Y. T. Long, Biological nanopores: Confined spaces for electrochemical single-molecule analysis. *Acc. Chem. Res.* **51**, 331–341 (2018).
5. X. Fan *et al.*, Sensitive optical biosensors for unlabeled targets: A review. *Anal. Chim. Acta* **620**, 8–26 (2008).
6. N. Toropov *et al.*, Review of biosensing with whispering-gallery mode lasers. *Light Sci. Appl.* **10**, 42 (2021).

7. H. Li, L. Shang, X. Tu, L. Liu, L. Xu, Coupling variation induced ultrasensitive label-free biosensing by using single mode coupled microcavity Laser. *J. Am. Chem. Soc.* **131**, 16612–16613 (2009).
8. F. Vollmer, S. Arnold, D. Keng, Single virus detection from the reactive shift of a whispering-gallery mode. *Proc. Natl. Acad. Sci. U.S.A.* **105**, 20701–20704 (2008).
9. M. D. Baaske, M. R. Foreman, F. Vollmer, Single-molecule nucleic acid interactions monitored on a label-free microcavity biosensor platform. *Nat. Nanotechnol.* **9**, 933–939 (2014).
10. J. Zhu *et al.*, On-chip single nanoparticle detection and sizing by mode splitting in an ultrahigh-q microresonator. *Nat. Photonics* **4**, 46 (2010).
11. L. Shao *et al.*, Detection of single nanoparticles and lentiviruses using microcavity resonance broadening. *Adv. Mater.* **25**, 5616–5620 (2013).
12. J. Su, A. F. G. Goldberg, B. M. Stoltz, Label-free detection of single nanoparticles and biological molecules using microtoroid optical resonators. *Light Sci. Appl.* **5**, e16001 (2016).
13. A. M. Armani, R. P. Kulkarni, S. E. Fraser, R. C. Flagan, K. J. Vahala, Label-free, single-molecule detection with optical microcavities. *Science* **317**, 783–787 (2007).
14. S. Arnold, S. I. Shopova, S. Holler, Whispering gallery mode bio-sensor for label-free detection of single molecules: Thermo-optic vs. reactive mechanism. *Opt. Express* **18**, 281–287 (2010).
15. N. P. Mauranyapin, L. S. Madsen, M. A. Taylor, M. Waleed, W. P. Bowen, Evanescent single-molecule biosensing with quantum-limited precision. *Nat. Photonics* **11**, 477–481 (2017).
16. X. C. Yu *et al.*, Optically sizing single atmospheric particulates with a 10-nm resolution using a strong evanescent field. *Light Sci. Appl.* **7**, 18003 (2018).
17. S. J. Tang *et al.*, On-chip spiral waveguides for ultrasensitive and rapid detection of nanoscale objects. *Adv. Mater.* **30**, e1800262 (2018).
18. H. Li *et al.*, Single-molecule detection of biomarker and localized cellular photothermal therapy using an optical microfiber with nanointerface. *Sci. Adv.* **5**, eaax4659 (2019).
19. M. Iqbal *et al.*, Label-free biosensor arrays based on silicon ring resonators and high-speed optical scanning instrumentation. *IEEE J. Sel. Top. Quantum Electron.* **16**, 654–661 (2010).
20. F. Liang, Y. Guo, S. Hou, Q. Quan, Photonic-plasmonic hybrid single-molecule nanosensor measures the effect of fluorescent labels on DNA-protein dynamics. *Sci. Adv.* **3**, e1602991 (2017).
21. Y. Sun, X. Fan, Optical ring resonators for biochemical and chemical sensing. *Anal. Bioanal. Chem.* **399**, 205–211 (2011).
22. J. M. Ward, N. Dhasmana, S. N. Chormaic, Hollow core, whispering gallery resonator sensors. *Eur. Phys. J. Spec. Top.* **223**, 1917–1935 (2014).
23. Z. Guo *et al.*, Ultra-sensitive biomolecular detection by external referencing optofluidic microbubble resonators. *Opt. Express* **27**, 12424–12435 (2019).
24. Z. Li *et al.*, Highly sensitive label-free detection of small molecules with an optofluidic microbubble resonator. *Micromachines (Basel)* **9**, 274 (2018).
25. L. T. Hogan *et al.*, Toward real-time monitoring and control of single nanoparticle properties with a microbubble resonator spectrometer. *ACS Nano* **13**, 12743–12757 (2019).
26. J. M. Ward *et al.*, Nanoparticle sensing beyond evanescent field interaction with a quasi-droplet microcavity. *Optica* **5**, 674–677 (2018).
27. Y. Yang, J. Ward, S. N. Chormaic, Quasi-droplet microbubbles for high resolution sensing applications. *Opt. Express* **22**, 6881–6898 (2014).
28. H. Li, Y. Guo, Y. Sun, K. Reddy, X. Fan, Analysis of single nanoparticle detection by using 3-dimensionally confined optofluidic ring resonators. *Opt. Express* **18**, 25081–25088 (2010).
29. D.-Q. Yang *et al.*, Operando monitoring transition dynamics of responsive polymer using optofluidic microcavities. *Light Sci. Appl.* **10**, 128 (2021).
30. S. I. Shopova, R. Rajmangal, S. Holler, S. Arnold, Plasmonic enhancement of a whispering-gallery-mode biosensor for single nanoparticle detection. *Appl. Phys. Lett.* **98**, 243104 (2011).
31. J. D. Swaim, J. Knittel, W. P. Bowen, Detection limits in whispering gallery biosensors with plasmonic enhancement. *Appl. Phys. Lett.* **99**, 243109 (2011).
32. P. Zijlstra, P. M. R. Paulo, M. Orrit, Optical detection of single non-absorbing molecules using the surface plasmon resonance of a gold nanorod. *Nat. Nanotechnol.* **7**, 379–382 (2012).
33. Q. Lu *et al.*, Strong coupling of hybrid and plasmonic resonances in liquid core plasmonic micro-bubble cavities. *Opt. Lett.* **40**, 5842–5845 (2015).
34. L. G. Guimarães, H. M. Nussenzveig, Theory of Mie resonances and ripple fluctuations. *Opt. Commun.* **89**, 363–369 (1992).
35. B. R. Johnson, Theory of morphology-dependent resonances: Shape resonances and width formulas. *J. Opt. Soc. Am. A* **10**, 343–352 (1993).
36. J. Liao, L. Yang, Optical whispering-gallery mode barcodes for high-precision and wide-range temperature measurements. *Light Sci. Appl.* **10**, 32 (2021).
37. M. R. Foreman, J. D. Swaim, F. Vollmer, Whispering gallery mode sensors. *Adv. Opt. Photonics* **7**, 168–240 (2015).
38. F. Vollmer, S. Arnold, D. Braun, I. Teraoka, A. Libchaber, Multiplexed DNA quantification by spectroscopic shift of two microsphere cavities. *Biophys. J.* **85**, 1974–1979 (2003).
39. F. Vollmer, S. Arnold, Whispering-gallery-mode biosensing: Label-free detection down to single molecules. *Nat. Methods* **5**, 591–596 (2008).
40. F. Vollmer, L. Yang, Label-free detection with high-Q microcavities: A review of biosensing mechanisms for integrated devices. *Nanophotonics* **1**, 267–291 (2012).
41. V. R. Dantham *et al.*, Label-free detection of single protein using a nanoplasmonic -photonic hybrid microcavity. *Nano Lett.* **13**, 3347–3351 (2013).
42. M. R. Foreman, W. L. Jin, F. Vollmer, Optimizing detection limits in whispering gallery mode biosensing. *Opt. Express* **22**, 5491–5511 (2014).
43. M. Jin *et al.*, 1/f-noise-free optical sensing with an integrated heterodyne interferometer. *Nat. Commun.* **12**, 1973 (2021).
44. B. Q. Shen *et al.*, Detection of single nanoparticles using the dissipative interaction in a high-q microcavity. *Phys. Rev. Appl.* **5**, 024011 (2016).
45. E. Kim, M. D. Baaske, F. Vollmer, In situ observation of single-molecule surface reactions from low to high affinities. *Adv. Mater.* **28**, 9941–9948 (2016).
46. S. Suebka, P. D. Nguyen, A. Gin, J. Su, How fast it can stick: Visualizing flow delivery to microtoroid biosensors. *ACS Sens.* **6**, 2700–2708 (2021).
47. P. E. Sheehan, L. J. Whitman, Detection limits for nanoscale biosensors. *Nano Lett.* **5**, 803–807 (2005).
48. X. Fan, I. M. White, Optofluidic microsystems for chemical and biological analysis. *Nat. Photonics* **5**, 591–597 (2011).
49. S. J. Tang *et al.*, A tunable optofluidic microlaser in a photostable conjugated polymer. *Adv. Mater.* **30**, e1804556 (2018).
50. M. Sumetsky, Y. Dulashko, R. S. Windeler, Optical microbubble resonator. *Opt. Lett.* **35**, 898–900 (2010).
51. W. Lee *et al.*, A quasi-droplet optofluidic ring resonator laser using a micro-bubble. *Appl. Phys. Lett.* **99**, 091102 (2011).